1

Dual-Periodic Photonic Crystal Structures

Alexey Yamilov and Mark Herrera[1]
Department of Physics, Missouri University of Science & Technology, Rolla, MO 65409, U.S.A.

1. Introduction

In this chapter we discuss optical properties of dual-periodic photonic (super-)structures. Conventional photonic crystal structures exhibit a periodic modulation of the dielectric constant in one, two or three spatial dimensions (Joannopoulos, 2008). In a dual-periodic structure, the dielectric constant is varied on two distinct scales $a_{1,2}$ along the same direction(s). An example of such a variation is given by the expression:

$$\varepsilon(x) = \varepsilon_0 + \Delta \times \left(1 + \gamma \cos\frac{2\pi}{a_1} x\right) \times \cos\frac{2\pi}{a_2} x. \quad (1)$$

In Sec. 2, after motivating our study, we describe one attractive possibility for a large-scale fabrication of the dual-periodic structures such as in Eq. (1) using the interference photo-lithorgraphy technique.
Sec. 3 presents the theory of slow-light effect in a dual-periodic photonic crystal. Here, four numerical and analytical techniques employed to study optical properties of the system. In the result, we obtain a physically transparent description based on the coupled-resonator optical waveguide (CROW) concept (Yariv et al., 1999).
Sec. 4 is devoted to discussion of a new type of optical waveguides – trench waveguide – in photonic crystal slabs. We demonstrate that this type of waveguide leads to an appearance of a second (super-) modulation in the slab, thus, slow-light devices / coupled-cavity micro-resonator arrays can be straightforwardly fabricated in the photonic crystal slab geometry. Importantly, the fabrication of such structures also does not require slow (serial) electron-beam lithography and can be accomplished with scalable (holographic) photolithography. The chapter concludes with a discussion and an outlook.

2. Dual-periodic structure as a photonic super-crystal

Optical pulse propagation in dielectrics is determined by the group velocity $v_g = d\omega(K)/dK$, where the dispersion $\omega(K)$ relates the frequency ω and the wave vector K inside the medium. One of the appealing features of photonic crystals has become a possibility to alter the dispersion of electromagnetic waves (Soukoulis, 1996) so that in a certain spectral region v_g becomes significantly smaller than the speed of light in vacuum. This "slowlight" effect (Milonni, 2005) attracted a great deal of practical interest because it can lead to low-threshold lasing (Nojima, 1998; Sakoda, 1999; Susa, 2001), pulse delay(Poon et al., 2004;

[1] Currently at department of Physics, University of Maryland

Source: Recent Optical and Photonic Technologies, Book edited by: Ki Young Kim,
ISBN 978-953-7619-71-8, pp. 450, January 2010, INTECH, Croatia, downloaded from SCIYO.COM

Vlasov et al., 2005), optical memories (Scheuer et al., 2005), and to enhanced nonlinear interactions (Soljacic et al, 2002; Xu et al., 2000; Jacobsen et al., 2006). Several approaches to obtaining low dispersion in photonic crystal structures have been exploited:

i. At frequencies close to the photonic band-edge, $\omega(K)$ becomes flat and group velocity approaches zero due to the Bragg effect at the Brillouin zone boundary. This property has been extensively studied and used in practice to control the spontaneous emission (Yablonovitch, 1987) and gain enhancement in lasers (Nojima, 1998; Sakoda, 1999; Susa, 2001). However, a large second order dispersion (i.e. dependence of v_g on frequency) in the vicinity of the bandedge leads to strong distortions in a pulsed signal that makes this approach unsuitable for, e.g., information processing applications.
ii. High order bands in two- and three-dimensional photonic crystals can have small dispersion not only at the Brillouin zone boundary but also throughout the band (Galisteo-López & López, 2004; Scharrer et al., 2006) where the second order dispersion can be significantly reduced. Nevertheless, these high-frequency photonic bands allow little control over v_g and are not spectrally isolated from other bands. These drawbacks and the increased sensitivity to fabrication errors (Dorado et al., 2007), limit the practical value of this approach.
iii. Based on the Coupled Resonator Optical Waveguide idea (CROW)(Stefanou & Modinos, 1998; Yariv et al., 1999; Poon et al., 2006; Scheuer et al., 2005), a low-dispersion photonic band can be purposefully created via hybridization of high-Q resonances arising from periodically positioned structural defects (Bayindir et al., 2001a;b; Altug & Vuckovic, 2005; Olivier et al., 2001; Karle et al., 2002; Happ et al., 2003; Yanik & Fan, 2004). This *spectrally isolated* defect-band is formed inside the photonic bandgap, with a dispersion relation given by

$$\omega(K) = \Omega[1 + \kappa\cos(KL)]. \tag{2}$$

Here Ω is the resonance frequency for a single defect, κ is the coupling constant (assumed to be small) and L is the spacing between defects. These adjustable parameters allow one to control the dispersion in the band, and hence v_g, without significant detrimental effects associated with the second order dispersion.

A periodic arrangement of structural defects in the photonic crystal, described in (iii), creates a dual-periodic *photonic super-crystal* (PhSC) with short-range quasi-periodicity on the scale of the lattice constant and with long-range periodicity on the defect separation scale (Shimada et al., 2001; Kitahara et al., 2004; Shimada et al., 1998; Liu et al., 2002; Sipe et al., 1994; Benedickson et al., 1996; Bristow et al., 2003; Janner et al., 2005; Yagasaki et al., 2006). These structures usually need to be constructed with the layer-by-layer technique (or, more generally, serially) which is susceptible to the fabrication errors similarly to the other approaches (i,ii) above. We have recently proposed a PhSC with dual-*harmonic* modulation of the refractive index (Yamilov & Bertino, 2007), similar to Eq. (1), that can be fabricated by e.g. a single-step interference photolithography technique (Bertino et al., 2004; 2007). We considered four S-polarized laser beams defined by

$$\begin{bmatrix} \mathbf{q}_{L1}, E_{L1} \\ \mathbf{q}_{L2}, E_{L2} \\ \mathbf{q}_{R1}, E_{R1} \\ \mathbf{q}_{R2}, E_{R2} \end{bmatrix} = \begin{bmatrix} k_0\{-\sin(\theta_1), 0, \cos(\theta_1)\}, E_1 \\ k_0\{-\sin(\theta_2), 0, \cos(\theta_2)\}, E_2 \\ k_0\{\sin(\theta_1), 0, \cos(\theta_1)\}, E_1 \\ k_0\{\sin(\theta_2), 0, \cos(\theta_2)\}, E_2 \end{bmatrix}. \tag{3}$$

Here **q** and E are the k-vector and amplitude of the beams respectively. Their interference pattern $E_{tot}(x) \propto \alpha\cos(k_1 x) + \beta\cos(k_2 x)$ leads to

$$n^2(x) = \varepsilon(x) = \varepsilon_0 + \Delta\varepsilon\left[\alpha\cos(k_1 x) + \beta\cos(k_2 x)\right]^2 \tag{4}$$

where $k_1 - k_2 \equiv \Delta k$, $(k_1 + k_2)/2 \equiv k$ and $\alpha + \beta = 1$. k and Δk are related to the short (a_S) and long range modulations of the refractive index: $a_S = 2\pi/\Delta k$, $a_L = \pi/k$. The parameters in Eqs. (3, 4) are related as $\alpha = E_1/(E_1 + E_2)$, $\beta = E_2/(E_1 + E_2)$ and $k_1 = k_0 \sin\theta_1$, $k_2 = k_0 \sin\theta_2$. Manipulation of the beams allows for an easy control over the structural properties of the resultant PhC: (i) fundamental periodicity a_S via k_0 and $\theta_{1,2}$; (ii) long-range modulation a_L via $\theta_1 - \theta_2$; and (iii) depth of the long-range modulation via relative intensity of the beams E_1/E_2. As we demonstrate in Sec. 3, the longer range modulation accomplishes the goal of creating the periodically positioned optical resonators. The condition of weak coupling $\kappa \ll 1$ between the states of the neighboring resonators requires sufficiently large barriers and therefore $a_S \ll a_L$, which we assume hereafter. Our approach to making dual-periodic structures has an advantage in that all resonators are produced at once and, therefore, it minimizes fabrication error margin and ensures the large-scale periodicity essential for hybridization of the resonances of individual cavities in an experiment.

Dual-periodic harmonic modulation of the refractive index can also be experimentally realized in optically-induced photorefractive crystals (Fleischer et al., 2003; Neshev et al., 2003; Efremidis et al., 2002). Although, the index contrast obtained is several orders of magnitude less than with QDPL (Bertino et al., 2004; 2007), the superlattices created in photorefractive materials offer a possibility of dynamical control – a feature lacking in the quantum dot system. While the study of dynamical and nonlinear phenomena in dual-periodic lattices is of significant interest, it goes beyond the scope of our study and will not be considered in this work.

3. Theory of slow-light effect in dual-periodic photonic lattices

In this section we theoretically investigate the optical properties of a one-dimensional PhSC using a combination of analytical and numerical techniques. We consider the dielectric function of the form given in Eq. (1) that can be produced with the interference photolithography method:

$$\varepsilon(x) = \varepsilon_0 + \frac{\Delta\varepsilon/2}{1+\gamma}\left[1 + \gamma\cos\left(2\pi x/L\right)\right]\left[1 + \cos\left(2\pi x/a\right)\right]. \tag{5}$$

Here ε_0 is the background dielectric constant. The amplitude of the short-range (on scale a) modulation gradually changes from $\Delta\varepsilon \times (1 - \gamma)/(1 + \gamma)$ to $\Delta\varepsilon$, c.f. Fig. 1a. $L = Na$ sets the scale of the long-range modulation, $N \gg 1$ is an integer.

The functional form in Eq. (5) was chosen to enable an analytic treatment and differs slightly from Eq. (4). Nonetheless, it shows the same spectral composition and modulation property. The discrepancy between the two forms is expected to cause only small deviations from the analytical results obtained in this section. Furthermore, the differences become insignificant in the limit $N \gg 1$.

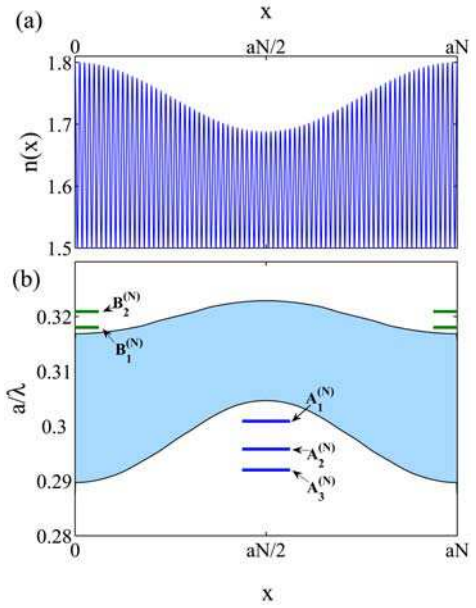

Fig. 1. (a) Dependence of the index of refraction in a dual-periodic photonic crystal as defined by Eq. (5). We used $\varepsilon_0 = 2.25$, $\Delta\varepsilon = 1$, $N = 80$ and the modulation parameter γ is equal to 0.25. (b) Local (position-dependent) photonic bandgap diagramfor $n(x)$ in (a). $A_i^{(N)}$ and $B_i^{(N)}$ mark the frequencies of the foremost photonic bands on the long- and short-wavelength sides of the photonic bandgap of the corresponding single-periodic crystal.

3.1 Transfer matrix analysis and coupled-resonators description of PhSC

The transmission/reflection spectrum of a one-dimensional PhSC of finite length, and the band structure of its infinite counterpart can be obtained numerically via the transfer matrix approach. Propagation of a field with wavevector $k = \omega/c$ through an infinitesimal segment of length dx is described by the transfer matrix (Yeh, 2005)

$$\widehat{M}(x, x+xd) = \begin{bmatrix} \cos(kn(x)dx) & n^{-1}(x)\sin(kn(x)dx) \\ -n(x)\sin(kn(x)dx) & \cos(kn(x)dx) \end{bmatrix} \tag{6}$$

where we have assumed that the refractive index $n(x)$ does not change appreciably over that distance. The matrix $\widehat{M}(x, x + dx)$ relates the electric field and its spatial derivative $\{E, 1/k\, dE/dx\}$ at $x + dx$ and x. The total transfer matrix of a finite system is then given by the product of individual matrices

$$\widehat{M}_{tot} = \prod_{x=0}^{L} \widehat{M}(x, x+dx). \tag{7}$$

Since in our case the refractive index $n(x) = \varepsilon^{1/2}(x)$, Fig. 1(a), is not a piece-wise constant (in contrast to Refs. (Sipe et al., 1994; Benedickson et al., 1996)) but rather a continuous function of coordinate, one has to resort to numerical simulations. In what follows, we apply either

scattering or periodic boundary conditions to obtain the transmission coefficient and Bloch number $K(\omega)$ respectively.

Figure 2(a) plots the transmission coefficient through one period of the dual-periodic system shown in Fig. 1. A series of progressively sharper resonances occur on the lower or upper edge of the spectral gap of the underlying single-periodic structure. Whether the peaks occur at the lower or upper band edge depends on the particular definition of the unit cell, as shown in the inset of Fig. 2(a). One can gain an insight into this effect by examining the modulation of the spectral position of the "local" photonic bandgap (PBG) with the position as shown in Fig. 1(b). This analysis is meaningful on the length scale of the order $a \ll \Delta x \ll L \equiv Na$. This condition can be satisfied in our case of slow modulation, with large N. At frequencies such as $A_i^{(N)}$ in Fig. 1(b), wave propagation is allowed in the vicinity of $x = aN \times (1/2 + m)$, whereas at the regions $x = aN \times m$, with m being an integer, it is locally forbidden. When considering a segment of the lattice with $0 < x < Na$, resonant tunneling via electromagnetic states $A_i^{(N)}$ of the cavity at the geometrical center leads to low-frequency peaks in the transmission coefficient, indicated by the solid line in Fig. 2(a). On the other hand, transmission through the segment $-Na/2 < x < Na/2$ exhibits a series of sharp resonances. These correspond to tunneling via $B_i^{(N)}$ cavity states in the high-frequency region.

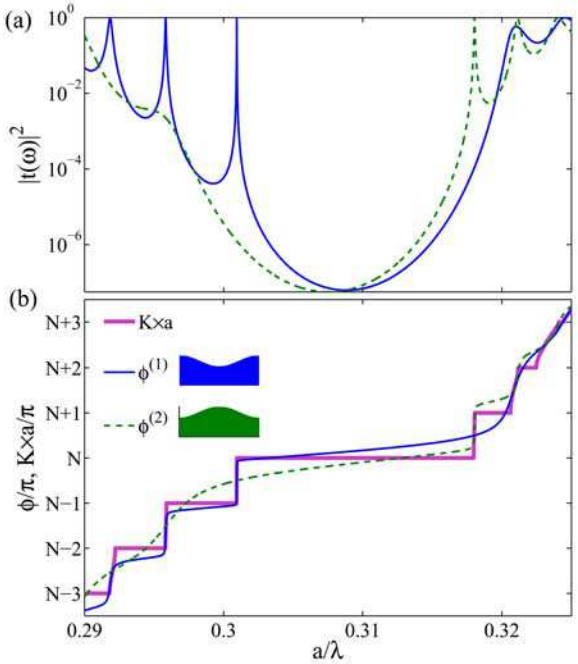

Fig. 2. (a) Transmission coefficient through a finite segment of length L (one period) of the periodic super-structure defined in Fig. 1. Solid and dashed lines correspond to $0 < x < Na$ and $-Na/2 < x < Na/2$ segments (shown in the inset of panel (b)) respectively. (b) Solid and dashed thin lines plot the corresponding phase of $t(\omega)$. Bold line depicts the Bloch number $K(\omega) \times a$ of the infinite crystal computed using Eq. 8.

The transmission coefficient through a finite segment of length L (equal to one period) can be related to the band structure of the corresponding periodic lattice (Benedickson et al., 1996) as

$$\cos(K(\omega)L) = Re[\frac{1}{t(\omega)}] \equiv \frac{1}{|t(\omega)|}\cos(\phi(\omega)), \tag{8}$$

where we have introduced the phase of the transmission coefficient $\phi(\omega)$ through $t = |t|\exp[i\phi]$. Fig. 3 shows that hybridization of the cavity resonances considered above leads to the formation of flat photonic bands. Their low dispersion and small group velocity may be exploited (Yamilov & Bertino, 2007) for practical applications.

In the vicinity of an isolated transmission resonance, $t(\omega)$ is given by the Lorentzian

$$t(\omega) = \frac{(-1)^N(\Gamma/2)}{i(\Gamma/2) - (\omega - \omega_0)} \tag{9}$$

where Γ is the full width at half maximum (FWHM) of the resonance and ω_0 is the resonant frequency. Substitution of Eq. 9 into Eq. 8 gives the flat band described by

$$\omega(K) = \omega_0[1 \pm \kappa\cos(KL)] \tag{10}$$

where $\kappa = \frac{\Gamma}{2\omega_0} = \frac{1}{Q} \ll 1$, and Q is the cavity Q-factor. Thus, the decrease of group velocity in the PhSC is directly related to the increase of confinement and the decrease of coupling between neighboring cavities. In our PhSC both these factors are described by the same parameter – the cavity Q-factor. In a single-periodic photonic crystal of finite length, the Q-factor of a band-edge mode depends on the system size. Comparing Fig. 1(b) and Fig. 3, one can see that $A_i^{(N)}$, $B_i^{(N)}$ modes are in fact band edge modes in their intervals of free propagation.

In our case L gives the characteristic length and as we demonstrate below, also determines the mode frequency. As N increases, the eigenfrequencies of the modes shift towards the bandgap. The associated decrease of the local group velocity contributes to an increase of the Q-factor of the resonators and to a further reduction of the group velocity in $A_i^{(N)}$, $B_i^{(N)}$ bands in the $N \to \infty$ limit.

Eq. (8) suggests that the dispersion relation $\omega(K)$ is independent of how the segment of length L (the period of our structure) is chosen. However, the transmission coefficient through the $0 < x < Na$ and $-Na/2 < x < Na/2$ segments of the crystal shows very different spectral composition, Fig. 2(a). In order to understand how these markedly different functions lead to the same $\omega(K)$, we analyze the phase of the transmission coefficient ϕ, shown in Fig. 2(b).

In a one-dimensional periodic system such as ours, the wave number $K(\omega)$ in Eq. 8 is equal to the integrated density of electromagnetic states. It is, by definition, a monotonically increasing function of frequency in the extended Brillouin zone scheme. In PhSC, $K \times L$ increases by π every time the frequency is increased through an allowed band, c.f. bold line in Fig. 2(b). At the frequency in the middle of the band, $\cos(KL) = 0$ because $K \times L = \pi \times (m + 1/2)$. From Eq. (8) one can see that ϕ should be equal to $\pi \times (m+1/2)$ at the same frequency. In the finite system, the mode counting phase $\tilde{\phi}$ defined (Lifshitz et al., 1998) as

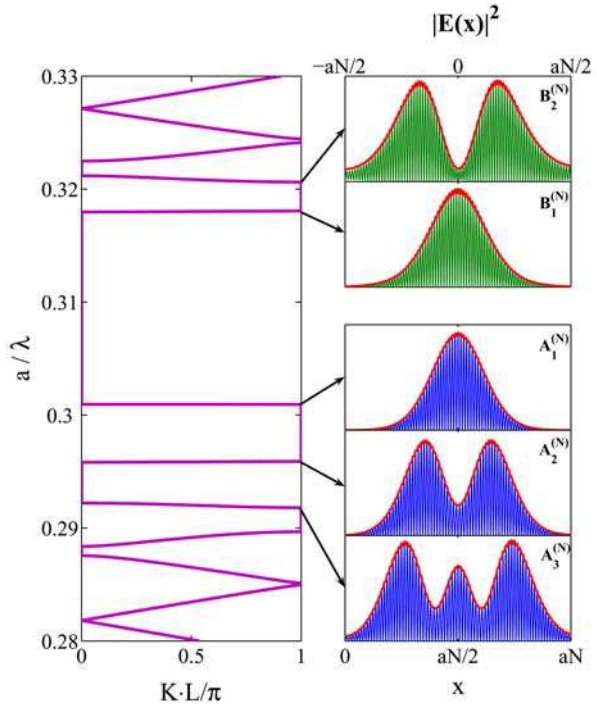

Fig. 3. The left panel shows dispersion of a PhSC $\omega(K)$ reduced to the first Brillouin zone. The eigenmodes which correspond to the series of flat bands in the vicinity of the parent-bandgap of the single periodic crystal are depicted on the right. Calculations were performed for the structure described in Fig. 1.

$\tan(\tilde{\phi}) = E'/E$ coincides with the phase of the transmission coefficient $\phi \equiv \tilde{\phi}$. This explains the monotonic behavior of $\phi(\omega)$. Eq. (8) leads to the fact that quasi-states of the finite system occur at the same place as the corresponding band center of the lattice, irrespective of the definition of the unit cell. Therefore, as can be also seen from Fig. 2(b), $\phi(\omega)$ and $K(\omega)L$ intersect at $\pi \times (m + 1/2)$.

Taylor expansion of the phase around the frequency ω_0 at the center of a pass band, where $K(\omega)L = \pi \times (m + 1/2)$ gives

$$\cos(K(\omega)L) = (\omega - \omega_0) \times \frac{(-1)^m}{|t(\omega_0)|} \frac{d\phi(\omega_0)}{d\omega}. \tag{11}$$

Here, the term that contained $d\,|t(\omega_0)|/d\omega$ dropped out because $\cos(K(\omega_0)L) = 0$. Comparing Eqs. (10) and (11) shows that it is $|t(\omega_0)|^{-1}\, d\phi(\omega_0)/d\omega$ that determines $Q = 1/\kappa$ and not just $|t(\omega_0)|$. Suppressed transmission compensates for a slow phase change (e.g. solid line in Fig. 2(b) in the high frequency spectral region) and leads to an identical $K(\omega)$ for two different definitions of the unit cell.

We also note that if the segment is chosen such that the corresponding "cavity" is located in the geometrical center ($|t(\omega_0)| = 1$), the FWHM of the resonance (Γ) in the transmission

coefficient is equal to the width of the pass band in the periodic lattice. This fact follows from Eqs. (8) and (9). It further emphasizes the analogy with CROW structures.

We conclude this section by reiterating that long-range refractive index modulation creates alternating spatial regions which serve as resonators separated by the tunneling barriers. Hybridization of the cavity resonances creates a series of photonic bands with low dispersion. The envelope of the eigenstates in these bands $A_i^{(N)}$, $B_i^{(N)}$ is a slowly varying function of the coordinate, c.f. Fig. 3. This effect stems from states proximity to the photonic band-edge of the underlying single-periodic lattice. The possibility of a separation into short (a of rapid field oscillations) and long (L of the slow amplitude variation) length scales will further inform analytical studies presented in the following sections.

In addition, the results of this section lead to somewhat counter-intuitive conclusion that the larger or even complete modulation in Eq. (5) would negatively affect (increase) the coupling between the resonators. This can also be seen from PBG diagram in Fig. 1b: in case of compete modulation of the refractive index ($\gamma = 1$), the local bandgap disappears at $x_m = aN \times (1/2 + m)$. Indeed, our photonic band structure calculations demonstrate that structures with 100% modulation are less advantageous and lead to significantly larger propagation speeds. The optimum value of γ depends on the experimental parameters (ε_0, $\Delta\varepsilon$ and N) and should be determined with the help of PBG diagram similar to Fig. 1b. The diagram also proves useful in explaining the advantage of A_N over B_N. In the latter case, the tunneling barriers are thinner and their localization length is longer (PBG is spectrally narrower at $x_m = aN \times (1/2 + m)$ than it is at $x_m = aN \times m$).

3.2 Resonant approximation

Forbidden gaps in the spectra of a periodic system arise due to a resonant interaction of the wave with its Bragg-scattered counterpart (Ashcroft & Mermin, 1976). The scattered wave appears due to the presence of Fourier harmonics in the spectrum of the periodic "potential", which in the case of the Helmholtz equation

$$E''(x) + \frac{\omega^2}{c^2}\delta\varepsilon(x)E(x) = \frac{\omega^2}{c^2}\bar{\varepsilon}E(x), \tag{12}$$

is represented by $(\omega^2/c^2)\delta\varepsilon(x) \equiv (\omega^2/c^2)\left[\varepsilon(x) - \bar{\varepsilon}\right]$. Here we have introduced the average value of the dielectric function $\bar{\varepsilon} = \overline{\varepsilon(x)} = \varepsilon_0 + \Delta\varepsilon/[2(1+\gamma)]$. When $\gamma = 0$, the condition $\Delta\varepsilon/\bar{\varepsilon} \ll 1$ is sufficient to obtain the position and width of spectral gaps. Otherwise, an additional condition $N \times \Delta\varepsilon/\bar{\varepsilon} \ll 1$ needs to be satisfied instead. We will discuss the physical meaning of this condition at the end of this section.

We begin by noticing that $\delta\varepsilon(x)$ of our choice (Eq. 5) contains only eight nonzero Fourier harmonics:

$$\varepsilon(x) = \sum_{m=-\infty}^{\infty} \varepsilon_m \exp\left[i\frac{2\pi}{L}mx\right], \tag{13}$$

where $m = \{\pm 1, \pm(N-1), \pm N, \pm(N+1)\}$. This fact allows for an exhaustive study of all resonant interactions as follows. Expressing $E(x)$ in terms of its Fourier components

$$E(x) = \exp[iK(\omega)x] \sum_{m=-\infty}^{\infty} E_m \exp\left[i\frac{2\pi}{L} mx \right] \tag{14}$$

leads to an infinite system of linear coupled equations

$$\left[\frac{\omega^2}{c^2}\bar{\varepsilon} - \left(K(\omega) + \frac{2\pi}{L} m \right)^2 \right] E_m + \frac{\omega^2}{c^2} \sum_{m' \neq 0} \varepsilon_{m'} E_{m-m'} = 0, \tag{15}$$

where K is the Bloch number that varies in the first Brillouin zone $[0, \pi/L]$. For the extreme values of K there exists a spectral range where the term in brackets in Eq. 15 can become simultaneously small for certain values of m and $-m$ at $K = 0$, and for m and $-m - 1$ at $K = \pi/L$. If $\varepsilon(x)$ contains a harmonic $\varepsilon_{m'}$ such that it couples these two Fourier components, the overall infinite system Eq. 15 can be reduced to two resonant equations.

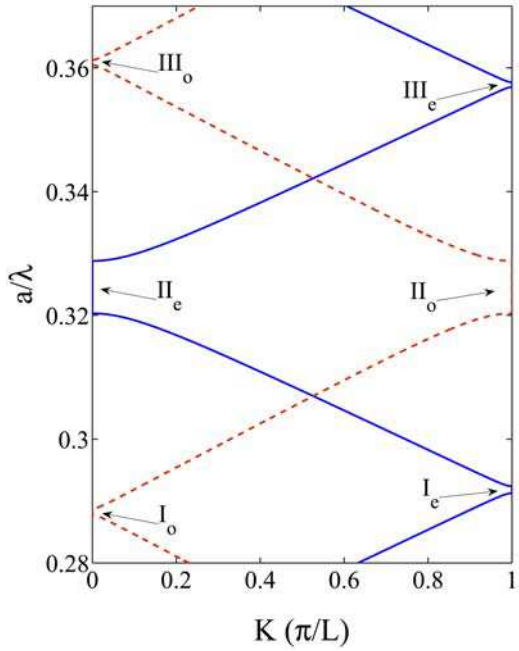

Fig. 4. Dispersion relation computed with the transfer matrix formalism for $\varepsilon_0 = 2.25$, $\Delta\varepsilon = 0.32$, $N = 9$ (dashed line) and $N = 10$ (solid line). The modulation parameter γ is equal to 0.25. For this set of parameters, the applicability condition Eq. 16 of the resonant approximation is satisfied.

The results of such an analysis are summarized in Table 1 and the corresponding band structure is shown in Fig. 4. Introduction of the long range modulation in the dielectric constant results in an expansion of the unit cell from a to $L = Na$ and, thus, to a reduction of the Brillouin zone, accompanied by the folding of photonic bands. The cases of even $N = 2s$ and odd $N = 2s + 1$ should be distinguished. In the former, the primary photonic bandgap (II_e) of the single-periodic lattice reappears at $K = 0$, whereas in the latter (II_o) it is located at

$K = \pi/L$. Our analysis shows that the nearest frequency gaps, $I_{o,e}$ and $III_{o,e}$, also become resonant, Fig. 4. For the refractive index modulation of Eq. (5), the normalized width $\varepsilon_{(N-1)} / \bar{\varepsilon} = \dfrac{\gamma\Delta\varepsilon / 4\bar{\varepsilon}}{1+\gamma}$ of the satellite gaps is smaller than that of the central gap by a factor of γ. By definition, this parameter is less than unity.

We can see that folding and the offset of the formation of flat $A_1^{(N)}$, $B_1^{(N)}$ bands is captured in this approximation. The criterion of its applicability can be found by considering the contributions of non resonant terms in Eq. (15). We find that for all three gaps the criteria are qualitatively the same. Therefore, we present the detailed analysis of only one particular resonance, III_e. The condition that the closest non-resonant Fourier components E_{-s-2}, E_{-s}, E_{s-1} and E_{s+1} be smaller than the resonant ones E_{-s-1} and E_s leads to the relation

$$\frac{(N+1)^2(\varepsilon_1+\varepsilon_N)}{4N\bar{\varepsilon}+2(N+1)^2\varepsilon_{N-1}} \ll 1. \tag{16}$$

In the limit of very large N the second term in the denominator becomes dominant and this condition cannot be satisfied for any value of $\Delta\varepsilon$. Thus, N should be finite. The condition that the first termin the denominator be dominant, is consistent with the entire inequality Eq. (16), and is equivalent to $N\varepsilon_i / \bar{\varepsilon} \ll 1$. Taking the most restrictive case for ε_i, we finally obtain

$$\frac{\Delta\varepsilon}{8\bar{\varepsilon}} \times N \ll 1, \tag{17}$$

where we have neglected γ for simplicity.

Equation (17) has a clear physical meaning. Indeed, from Table 1, it is clear that the frequency of bandgaps I and III approach the central gap inherited from the single periodic system as $1/N$. At some point, a bandgap of width $\Delta\omega/\omega_0 = \varepsilon_i/\bar{\varepsilon}$ begins to substantially perturb the pass band of width $K_{max} \times c \simeq \omega_0/N$ separating consecutive gaps. The resonant approximation breaks when these two scales become comparable. This condition results in Eq. (17). In other words, the approximation considered in this section can at most capture the onset of the flattening trend in the $A_1^{(N)}$, $B_1^{(N)}$ bands and fails when N is increased to the point where these states become abnormally flat, i.e., where $\Delta\omega/K_{max} \ll c/\bar{\varepsilon}$ throughout the band. More sophisticated approaches are considered below.

Resonant K, (even N)	π/L	0	π/L
(odd N)	0	π/L	0
Coupled components	$E_{-s}, E_{N-(s+1)}$	E_{s-N}, E_s	$E_{-(s+1)}, E_{N-s}$
Coupling harmonics	$\varepsilon_{-(N-1)}, \varepsilon_{N-1}$	$\varepsilon_{-N}, \varepsilon_N$	$\varepsilon_{-(N+1)}, \varepsilon_{N+1}$
Center frequency, ω_0	$\dfrac{c\pi}{\sqrt{\bar{\varepsilon}}L}(N-1)$	$\dfrac{c\pi}{\sqrt{\bar{\varepsilon}}L}N$	$\dfrac{c\pi}{\sqrt{\bar{\varepsilon}}L}(N+1)$
Normalized width, $\Delta\omega/\omega_0$	$\varepsilon_{(N-1)}/\bar{\varepsilon}$	$\varepsilon_N/\bar{\varepsilon}$	$\varepsilon_{(N+1)}/\bar{\varepsilon}$

Table 1. Results of resonant approximation analysis of Eq. (15) with dielectric function given by Eq. (5). Three columns correspond to the three resonant photonic band gaps that appear in the spectrum of the dual-periodic PhSC. The expressions hold for both even and odd N for the choice of parameter s: $N = 2s$ and $N = 2s + 1$ respectively.

3.3 Effective medium approximation

Gratings written in the core of photosensitive optical fibers are often analyzed with the help of coupled-mode theory (CMT) (Marcuse, 1991). In both shallow gratings with long-range modulation in fibers (Sipe et al., 1994; Janner et al., 2005) and in our PhSC, the forward and backward (locally) propagating waves continuously scatter into each other. The advantage of CMT is that it considers the amplitudes of the forward and backward waves directly. This tremendously simplifies Maxwell equations. Ref. (de Sterke, 1998) also considered fiber gratings with a deep piece-wise constant index modulation. In this section we employ the CMT-based method developed by Sipe, *et al.* (Sipe et al., 1994) to obtain the spectral positions of the flat photonic bands formed in a PhSC.

For *shallow modulation*, i.e., small $\Delta\varepsilon$, our Eq. (5) can be brought to resemble the model function considered in Ref. (Sipe et al., 1994)

$$n(x)/n_0 = 1 + \sigma(x) + 2\kappa(x)\cos\left[2k_0 x + \varphi(x)\right] \tag{18}$$

with the following choice of parameters

$$\sigma(x) = \frac{\dfrac{\gamma\Delta\varepsilon/4}{1+\gamma}}{\varepsilon_0 + \dfrac{\Delta\varepsilon/2}{1+\gamma}} \times \cos\frac{2\pi}{L}x;$$

$$\kappa(x) = \frac{\dfrac{\Delta\varepsilon/8}{1+\gamma}}{\varepsilon_0 + \dfrac{\Delta\varepsilon/2}{1+\gamma}} \times \left(1 + \gamma\cos\frac{2\pi}{L}x\right); \tag{19}$$

$$\varphi(x) \equiv 0; \quad n_0 = \left(\varepsilon_0 + \frac{\Delta\varepsilon/2}{1+\gamma}\right)^{1/2}; \quad k_0 = \pi/a.$$

The CMT of Ref. (Sipe et al., 1994) is applicable as long as these functions have *a slow dependence on x*, on the scale much larger than k_0^{-1}. This condition is indeed satisfied in the PhSC with $N \gg 1$.

By introducing small detuning parameter

$$\delta = \frac{\omega - \omega_0}{\omega_0} \ll 1, \quad \omega_0 = \frac{k_0 c}{n_0}$$

we can, following Ref. (Sipe et al., 1994), obtain the governing equation for the quantity E_{eff} related to the envelope of the electric field

$$\frac{d^2 E_{eff}}{dx^2} + k_0^2 n_{eff}^2(x,\omega) E_{eff} = 0. \tag{20}$$

Frequency and position dependent effective refractive index

$$n_{eff} = \{(\sigma(x) + \Delta)^2 - \kappa(x)^2\}^{1/2} \tag{21}$$

determines whether propagation is locally allowed (real n_{eff}) or forbidden (imaginary n_{eff}). This is similar to our definition of the local PBG diagram which we studied numerically in Section 3. Figure 5b compares CMT's region of evanescent propagation (solid lines) to the

numerical calculation (dashed lines). We attribute the relatively small discrepancy observed there to the assumption of shallow modulation made in arriving at Eq. (21).

Eq. (20) is formally similar to the Schrödinger equation. Our previous analysis shows that the single-period states associated with photonic bands $A_i^{(N)}, B_i^{(N)}$ are confined to the region of classically allowed propagation, in the language of quantum mechanics. By analogy, the Wentzel-Kramers-Brillouin (WKB) approximation of quantum mechanics can be applied (Sipe et al., 1994) to determine the quantization of energies inside our optical equivalent of a quantum well

$$I(\omega) = k_0 \int_{x_L}^{x_R} n_{eff}(x,\omega)dx = (m+1/2)\pi \tag{22}$$

in which x_L and x_R are, respectively, the left and right turning points defined by the condition $n_{eff}(x_{L,R},\omega) = 0$, m is an integer. The solid line in Fig. 5a depicts the value of the integral in Eq. (22), as a function of ω, obtained numerically. The filled circles denote the frequencies at which quantization condition Eq. (22) is satisfied. In a system with the parameters which we used for illustration in previous sections, the obtained solutions are in fair agreement with numerical results obtained with the transfer matrix approach described in Section 3. This suggests that the index variation given by $\Delta\varepsilon = 1$, $\varepsilon_0 = 2.25$ was sufficiently small for this approach to still be qualitatively applicable.

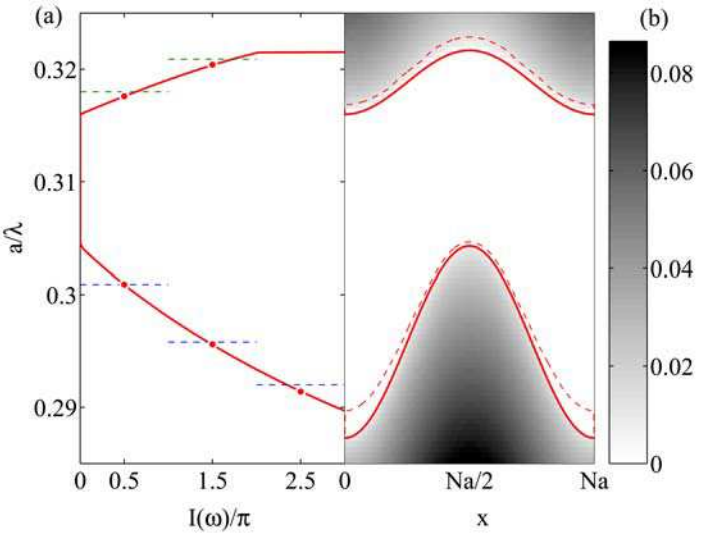

Fig. 5. (a) The value of the integral in Eq. (22), solid line, as a function of frequency is shown. For easy comparison with (b), the plot is transposed so that ω is plotted along the y-axis. The circles depict frequencies that satisfy the quantization condition of Eq. (22). The dashed lines denote the actual position of photonic states, as determined by direct numerical analysis of Section 3. (b) Gray-scale plot of $Re[n_{eff}(x,\omega)]$ given by Eq (21). The solid line shows the boundary of the regionwhere $Im[n_{eff}(x,\omega)] \neq 0$. For comparisonwe also show the local PBG of Fig. 1(b), dashed line. In both (a) and (b), the parameters of Fig. 1 are adopted.

We finish the current section by noting that it would be desirable to retain the attractive property of the CMT envelope approach without being constrained by the condition of small refractive index modulation. The latter may not always be justified in the experimental situation of interest (Bertino et al., 2004; 2007). In the following section we develop such an approach.

3.4 Bogolyubov-Mitropolsky approach

In this section we will consider the standing-wave solutions of Eq. (12). In this case, the corresponding $E(x)$ can be chosen to be a real function by an appropriate choice of normalization. Then, we make the Bogolyubov anzatz (Landa, 2001; Bogolyubov & Mitropolsky, 1974):

$$\begin{aligned} E(x) &= A(x)\cos\left(k_0 x + \phi(x)\right) \\ dE(x)/dx &= -k_0 A(x)\sin\left(k_0 x + \phi(x)\right), \end{aligned} \tag{23}$$

where, as in the preceding section, $k_0 = \pi/a$. The above equations define the amplitude and phase functions. Their substitution into Eq. (15) gives the so-called Bogolyubov equations in standard form (Landa, 2001; Bogolyubov & Mitropolsky, 1974)

$$\begin{aligned} \frac{d\phi(x)}{dx} &= \frac{1}{k_0}\left[\frac{\omega^2}{c^2}\varepsilon(x) - k_0^2\right]\cos^2\left(k_0 x + \phi(x)\right) \\ \frac{dA(x)}{dx} &= \frac{A(x)}{2k_0}\left[\frac{\omega^2}{c^2}\varepsilon(x) - k_0^2\right]\sin 2\left(k_0 x + \phi(x)\right), \end{aligned} \tag{24}$$

No approximations have been made so far. The structure of the above equation suggests that conditions $dA/dx \ll k_0 A$ and $d\phi/dx \ll k_0\phi$ can be satisfied in the vicinity of the spectral region where $(1/k_0)\left[\omega^2/c^2\overline{\varepsilon(x)} - k_0^2\right] \ll k_0$. Here, the overbar denotes an average over one period. Comparison with the analysis in the previous sections shows that this condition is satisfied in the vicinity of the primary photonic bandgap. In the system of interest, for which $N \gg 1$, this observation justifies the "averaging-out" of the fast spectral components, which is the Mitropolsky technique (Bogolyubov & Mitropolsky, 1974). This averaging procedure leads to the following system of nonlinear equations for the slow-varying amplitude and phase

$$\frac{d\phi(x)}{dx} = \frac{1}{2k_0}\left[\frac{\omega^2}{c^2}\varepsilon_0 - k_0^2 + \frac{\omega^2}{c^2}\frac{\Delta\varepsilon/2}{1+\gamma}\left(1+\gamma\cos\frac{2\pi}{L}x\right)\left(1+\frac{1}{2}\cos 2\phi(x)\right)\right] \tag{25}$$

$$\frac{d\log A(x)}{dx} = \frac{1}{2k_0}\frac{\omega^2}{c^2}\frac{\Delta\varepsilon/2}{1+\gamma}\left(1+\gamma\cos\frac{2\pi}{L}x\right)\sin 2\phi(x). \tag{26}$$

In deriving Eqs. (25) and (26) we have used the explicit form of $\varepsilon(x)$ given by Eq. (5).

We begin the analysis of Eqs. (25) and (26) with a discussion of the appropriate boundary conditions. In deriving these equations we have limited consideration to real-valued solutions of the original Eq. (15), which can be found only for a discrete set of frequencies. At these special frequencies, the corresponding amplitude function should reflect the periodicity of the dielectric function Eq. (5). This implies that

$$\phi(L) = \phi(0) + m\pi \tag{27}$$

$$\sin 2\phi(0, L/2, L) = 0. \tag{28}$$

The first condition is obtained by requiring $\sin 2\phi(x)$ in Eq. (26) to be periodic. Symmetry of the modulation profile $A(x)$, see Fig. 1(a), and continuity of its derivative lead to the condition $dA(x = 0, L/2, L)/dx = 0$. This can only be satisfied by requiring Eq. (28), because other factors on the right hand side of Eq. (26) are positive functions.

Equation (25) which determines the evolution of the phase is self-contained. Hence, its solution together with the constraints given by Eqs. (27) and (28) is sufficient to obtain the spectrum of the system and $\phi(x)$. The amplitude is to be recovered in the second step by simple integration of Eq. (26) with the found phase $\phi(x)$.

Figure 6 shows the solutions of the Eqs. (25, 26, 27, 28) obtained by a fourth order Runge-Kutta numerical method. In accord with our expectation, for each band there exist two solutions $\phi(x)$, which correspond to standing-wave band-edge modes at $K = 0, \pi/L$, as seen in Fig. 6a,e. The corresponding solutions of the amplitude equation, Fig. 6b-d, f-g, agree with the envelopes extracted from direct solutions of the Helmholtz equation, Fig. 3. The eigenvalues of Eq. (25) also give the frequencies that correspond to band-edge states, and

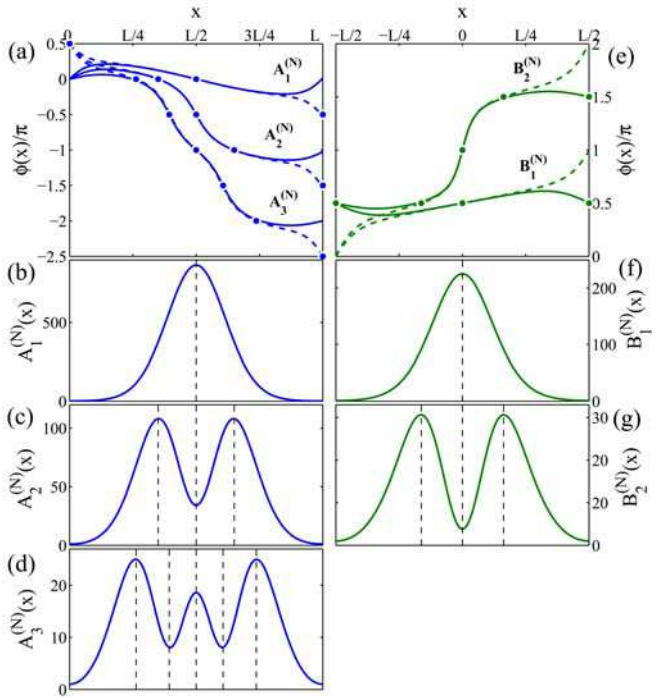

Fig. 6. Numerical solutions of Eqs. (25, 26, 27, 28) are shown. Filled circles in panels a,e denote the spatial position where the particular $\phi(x)$ is equal to $m\pi/2$. At these special points $dA(x)/dx = 0$ denoted by the vertical dashed lines in b-d and f-g panels. $A_i^{(N)}$ and $B_i^{(N)}$ denote the low-dispersion photonic bands as defined in Section 3.

are also in excellent agreement (the observed deviation is less than 0.1%), Fig. 3. Knowledge of the bandedge frequencies allows determination of all parameters of the tight-binding approximation for $\omega(K)$, Eq. (2). Therefore, the entire band structure in the spectral region of each of the flat bands can be obtained solely from solution of the amplitude-phase equation.
Filled circles in panels a,e of Fig. 6 denote the spatial position where the particular $\phi(x)$ is equal to $m\pi/2$. At these special points $dA(x)/dx = 0$, as denoted by the vertical dashed lines in b-d and f-g panels. Thus, the overall phase accumulated by $\phi(x)$ over one period is an important parameter indicative of the spatial structure of the amplitude. At the band-edge frequencies of the bands $A_1^{(N)}$ and $B_1^{(N)}$ (see Section 3 for notations), the phase is a bounded function $|\phi(x) - \phi(0)| \le \pi/2$. Therefore, $x = 0, L/2, L$ are the only positions where the corresponding amplitude function takes minimum/maximum values. Thus, as seen in Fig. 6b, f $A(x)$ has only one "hump" for $A_1^{(N)}$ and $B_1^{(N)}$. A comparison of $\phi(x)$ computed at the $K = 0$ (solid lines) and $K = \pi/L$ (dashed lines) edges of each photonic band shows (Fig. 6) that the difference occurs in the spatial regions where electromagnetic waves propagate via the "tunneling mechanism" in the language of CROWs of Section 3. In these regions $A(x)$ is small, which explains the small spectral width of the corresponding photonic bands.
As the eigenfrequencies of the higher order states $A_2^{(N)}, B_2^{(N)}$... shift further away from the primary band-gap region, Fig. 1b, $\phi(x)$ becomes progressively steeper function, leading to a steady increase in the number of "humps" in $A(x)$, Fig. 6. This progression accelerates the spatial dependence of the amplitude and leads to an eventual breakdown of the scale separation approximation used in the derivation of Eqs. (25) and (26). Nevertheless, such a loss of applicability occurs well outside the spectral region of interest, demonstrating the robustness of the approach developed here.

3.5 Comparison of theoretical approaches

Although all of the methods considered above have their limitations, the results obtained with each technique complement each other:
While numerical simulations with transfer matrices in Sec. 3.1 allow one to compute the photonic band structure for an arbitrary refractive index modulations, this method, however, may not provide a complete physical insight into the nature of the photonic bands. The transfer matrix approach allowed us to compare the spectrum of the infinite (periodic) crystal with the transmission spectrum of a finite system with a length equal to one period of the superstructure. We also were able to identify the individual transmission resonances with the photonic bands and found a one-to-one correspondence. Furthermore, the spatial distribution of the fields at resonance demonstrated that in the $L \gg a$ limit the envelope (amplitude) of the state changes slowly – on the scale of L.
With a method commonly employed in condensed matter physics, in Sec. 3.2 we investigated the resonant interactions between Bloch waves when the second, longer-scale, modulation is introduced. It was shown that the flattening of photonic bands is related to, but goes beyond band folding. The reduction in the group speed (slow-light effect) arises due to increased coupling between Bloch waves with k-vectors at the boundaries of the Brillouin zone. The subsequent increase of the band-gap regions "squeezes" the bands making them progressively flatter as $N = L/a$ is increased. Although, this approach fails for very large N, it still provides an important insight into the origin of the anomalously small dispersion in the spectra of PhSCs.

Diffraction gratings introduced in optical fibers are often spatially modulated. Coupled-mode theory has been developed to reduce the problem to a study of the amplitudes of the forward and backward propagating waves and to avoid a direct solution of Maxwell's equations. Although the method had been initially developed for optical fibers where the induced refractive index contrast is small, the CMT-based approach of Sec. 3.3 provided a clear physical picture. It showed that the electromagnetic states of our optical resonators can be thought of as eigenstates of the photonic wells. This further reinforced the analogy with CROWs that we developed in Sec. 3.1.

Noting a formal similarity between the Helmholtz equation with the considered dual-periodic dielectric function Eq. (5) and the equation describing parametric resonance in oscillation theory, we adopted an amplitude-phase formalism, accompanied by a separation of scales (short a and long $L = N \times a$), Sec. 3.4. In the result we were able to derive a tractable set of equations for the envelope functions. This enabled us to study physically meaningful mode profiles directly, without assuming small modulations of the refractive index.

4. Dual periodicity in trench waveguide in photonic crystal slab

4.1 Slow-light effect in photonic crystal slab

Photonic crystals have provided a way to control light on a sub-wavelength scale to an unprecedented degree (Joannopoulos, 2008). Particularly, the ability of photonic crystal slab (PhCS) waveguides (Johnson et al., 1999; 2000; Lončar et al., 2000) to control the propagation of light through photonic confinement makes them a versatile tool for use in a wide variety of practical applications (Chutinan & Noda, 2000; Krauss, 2003). The planar geometry of the PhCS waveguides makes it easy to incorporate them into larger scale integrated optical devices.

By changing the size of structural units (usually a cylindrical holes in a dielectric slab) or omitting them altogether along a row in the PhCS lattice, a spatially confined region is created where the local effective dielectric constant differs from that in the surrounding regions. Thus, a band-edge mode splits off from either the upper or lower photonic band and moves into the spectral interval of the photonic bandgap. This allows for the propagation of light at such frequencies but only within the confines of the perturbed region (Johnson et al., 2000; Lončar et al., 2000). In order to make such a waveguide, it is required to use electron-beam lithography to fabricate the carefully designed waveguide region of the PhCS as well as the rest of the structure, including the photonic crystal slab itself (Lončar et al., 2000). This technique becomes time intensive because each individual structural element in the device must be created serially – one element at a time.

Here we consider a PhCS-based waveguide design which can be implemented with a combination of a scalable and cost-effective laser holography (Cho et al., 2005; 2007) and photolithography techniques. We show that efficient waveguiding can be achieved by creating a shallow trench in the pre-patterned (e.g. holographically) PhCS blank. Making the slab locally thinner accomplishes the same goal of perturbing the local effective dielectric constant as in more conventional designs. Thus, the waveguiding effect along the trench in the photonic slab is achieved *without* changing the radius of the holes, or making other small-feature adjustments (such as displacements) to the holes. This observation shows that with the proposed design, one is no longer restricted to the use of e-beam lithography. Our study shows that this design yields robust structures, which are expected to be almost

insensitive to misalignment of the trench. At the same time, dispersion of the mode can be effectively tailored via adjustment of the trench width and its depth.
We note that the term "trench waveguide" was used by Yu. Vlasov and coworkers (Vlasov et al., 2004) in the context of a different structure – a uniform rectangular waveguide separated from PhCS's on both sides by small gaps (trenches).
We also make another observation, interesting from a conceptual point of view: unlike the guiding along a ridge which is also known in uniform (not PhCS) dielectrics, the guiding along a trench region is unique to the PhCS. In the latter system the vertical confinement does not originate from total internal reflection, but rather is related to the modifications of the optical dispersion due to the intrinsic periodicity in the PhCS.
Similar to other PhCS waveguides (when prepared on dielectric substrates), the trench waveguide suffers from propagation losses due to coupling between the guided mode and the bulk PhCS modes of the opposite parity (symmetry). In Sec. 4.2.3 we show that this effect is quite small in e.g. structures made of silicon. Thus, the trench waveguides could be used as an inexpensive alternative to carry optical signals over relatively short distances.
In Sec. 4.4 we demonstrate that when the trench waveguide is *rotated* with respect to the row of holes in the PhCS, the structure can be viewed as coupled-resonator optical waveguide (CROW) (Yariv et al., 1999) based on *dual-periodic photonic crystal* considered in Sec. 2,3. This makes our structures suitable for such applications as delay lines, optical storage, or coherently-coupled arrays of microlasers (Olivier et al., 2001; Karle et al., 2002; Yanik & Fan, 2004; Happ et al., 2003; Altug & Vučković, 2004).
Microlasers based on PhCS (Painter et al., 1999; Park et al., 2004) have attracted a great deal of attention due to low lasing thresholds and the possibility of on-chip integration. To increase the optical output and its efficiency, systems containing multiple coupled cavities were considered (Happ et al., 2003; Altug & Vučković, 2004). Usually, the efficiency of direct optical coupling between the microresonators is limited by the scalability of the fabrication process, as well as the ability to reliably reproduce cavities. In Sec. 4.4 we show that because different sections of the same (rotated) trench waveguide act as the optical cavities, the *resonator uniformity* is ensured. This feature of our design is expected to promote the optical coupling between individual resonators.

4.2 Formation of a guided mode in trench waveguide

4.2.1 Geometry

To investigate how the presence of a trench affects the optical properties of the PhCS, we computed the band structure $\omega_i(\vec{k})$ of several systems such as those shown in Fig. 7 with a plane-wave expansion method (Johnson & Joannopoulos, 2001). This method also provides us with the spatial distribution of the electric and magnetic fields at the eigen-frequency $\omega_i(\vec{k})$ found for the given wave vector $\vec{k}$. Because we are interested in the waveguiding properties of the structure, $\vec{k}$ will point in the direction of the trench.
In order to create a waveguiding channel, a line defect must be made in an existing photonic crystal slab. Rather than perturbing the shape/size of the holes, we alter the height of a linear region (stripe) of the material. Fig. 7 shows an example of one of the structures being considered. The system is a free-standing slab of silicon with a dielectric constant $\varepsilon_{slab} = 12.0$, and surrounding dielectric material of $\varepsilon_{air} = 1.0$. The dimensions of the structure are given in terms of the hexagonal lattice unit a, with the entire cell having dimensions of $2\sqrt{3}a \times 1a \times 4a$, which can be varied to achieve the desired level of accuracy. The radius of the